

Principal Component Analysis of SDSS Stellar Spectra

Rosalie C. McGurk, Amy E. Kimball, Željko Ivezić

Department of Astronomy, University of Washington, Box 351580, Seattle, WA 98195

ABSTRACT

We apply Principal Component Analysis (PCA) to $\sim 100,000$ stellar spectra obtained by the Sloan Digital Sky Survey (SDSS). In order to avoid strong non-linear variation of spectra with effective temperature, the sample is binned into 0.02 mag wide intervals of the $g - r$ color ($-0.20 < g - r < 0.90$, roughly corresponding to MK spectral types A3 to K3), and PCA is applied independently for each bin. In each color bin, the first four eigenspectra are sufficient to describe the observed spectra within the measurement noise. We discuss correlations of eigencoefficients with metallicity and gravity estimated by the Sloan Extension for Galactic Understanding and Exploration (SEGUE) Stellar Parameters Pipeline. The resulting high signal-to-noise mean spectra and the other three eigenspectra are made publicly available. These data can be used to generate high quality spectra for an arbitrary combination of effective temperature, metallicity, and gravity within the parameter space probed by the SDSS. The SDSS stellar spectroscopic database and the PCA results presented here offer a convenient method to classify new spectra, to search for unusual spectra, to train various spectral classification methods, and to synthesize accurate colors in arbitrary optical bandpasses.

Subject headings: stars: abundances – stars: statistics – methods: data analysis – stars: fundamental parameters

1. Introduction

A large number of homogeneously-obtained stellar spectra have recently become available. For example, the Sloan Digital Sky Survey (SDSS) (York et al. 2000) has made publicly available¹ over 460,000 stellar spectra as a part of its Data Release 7 (Abazajian & Sloan Digital Sky Survey

¹See <http://www.sdss.org/dr7>

2008), and Radial Velocity Experiments² (RAVE) may provide up to a million spectra over the next few years. This rapid progress in the availability of stellar spectra re-opens the old question of optimal stellar parameter extraction. For example, the SDSS estimates effective temperature, gravity, and metallicity using a variety of standard methods implemented in an automated pipeline (SEGUE³ Stellar Parameters Pipeline, hereafter SSPP; Beers et al. 2006). A detailed discussion of these methods and their performance can be found in Allende Prieto et al. (2006, 2007) and Lee et al. (2007a,b). The results of different methods implemented in the SSPP are *averaged* to obtain the final adopted values in the SDSS Spectral Parameter Pipeline table (*sppParams*). Although a detailed analysis by Lee et al. (2007a,b) demonstrates that systematic metallicity differences between the methods used in averaging do not exceed ~ 0.1 dex (with random errors in the range 0.1–0.3 dex), it is fair to ask whether a single method could be used to obtain the same level of systematic and random errors, instead of combining different methods with varying error properties.

Principal Component Analysis (PCA) has been demonstrated as a viable tool in solving this classification problem (Connolly et al. 1995; Connolly & Szalay 1998; Bailer-Jones et al. 1998; and references therein). Yip et al. (2004) have developed a PCA-based analysis code specialized to SDSS spectra. Here we use the same code to investigate whether the PCA eigencoeficients are correlated with the metallicity and gravity obtained by the SSPP. Byproducts of this analysis are high signal-to-noise eigenspectra that can be used to generate spectra for any combination of basic stellar parameters (effective temperature, metallicity, and gravity) within the parameter space probed by SDSS. Hence, given an arbitrary spectrum, one can attempt a low-dimensional fit using our library of eigenspectra. Among numerous drivers for such a library, we single out a photometric calibration scheme for the Large Synoptic Survey Telescope (LSST)⁴. LSST plans to use an auxiliary spectroscopic telescope to obtain spectra of standard stars at the same time as the main imaging survey is performed (see Ivezić et al. 2008b). The atmospheric transmission properties, required to photometrically calibrate the imaging survey, will be obtained by simultaneously fitting the stellar spectrum and a sophisticated atmospheric model with six free parameters for each observation. The ability to describe the expected stellar spectra in a low-dimensional continuous space by using a small number of eigencomponents, with eigencoeficients that are not defined on a fixed grid, might increase the fidelity of the fitted model.

In Section 2 we describe our sample selection and the application of PCA to SDSS stellar

²See <http://www.rave-survey.aip.de/rave>

³Sloan Extension for Galactic Understanding and Exploration

⁴See <http://www.lsst.org/>

spectra. We discuss our results in Section 3, and end with a summary in Section 4.

2. Principal Component Decomposition of SDSS Stellar Spectra

2.1. The properties of SDSS spectra

In addition to massive amounts of optical photometry of unprecedented quality, the SDSS has also produced a large spectroscopic database. A compendium of technical details about SDSS can be found on the SDSS web site⁵, which also provides an interface for public data access. Targets for the spectroscopic survey are chosen from the SDSS imaging data based on their colors and morphological properties (Strauss et al. 2002; Eisenstein et al. 2001; Richards et al. 2002). In the spectroscopic survey, stars are targeted either as calibrators or for scientific reasons in specific parts of the four-dimensional SDSS color space (Yanny et al. 2009).

A pair of multi-object fiber-fed spectrographs mounted onto the SDSS 2.5m telescope (Gunn et al. 2006) are used to take 640 simultaneous spectra within a radius of 1.49 degrees, each with wavelength coverage 3800–9200 Å and spectral resolution of ~ 2000 , and with a signal-to-noise ratio of >4 per pixel at $g=20.2$. Spectro-photometric calibration of these spectra is exquisite; for example, the imaging magnitudes and the stellar magnitudes synthesized from SDSS spectra agree with an rms of only ~ 0.05 mag (see Smolčić et al. 2004).

2.2. Sample selection

We begin by selecting bright stars in SDSS Data Release 6 that have colors consistent with the main stellar locus (Lenz et al. 1998; Fan 1999; Finlator et al. 2000), or are found in the regions populated by RR Lyrae stars (Ivezić et al. 2005) and blue horizontal branch stars (Sirko et al. 2004). Stars that are probable white dwarf — red dwarf pairs (Smolčić et al. 2004) or single hot white dwarfs (Eisenstein et al. 2006) are not selected. We only use stars from the sky regions with modest interstellar dust extinction, determined using the interstellar dust maps of Schlegel et al. (1998).

The specific criteria applied to 130,620 entries from the SDSS DR6 version of *sppParams*

⁵See <http://www.sdss.org/>

table⁶ that have $\log(g) > 0$ are (the number in brackets indicates the number of stars remaining after each selection step):

1. the interstellar extinction in the r band below 0.3; [106,816]
2. $14 < g < 19.5$; [104,844]
3. $-0.2 < g - r < 0.9$; [103,588]
4. $0.7 < u - g < 2.4$; [101,630]
5. $\{-0.2 < g - r - 0.5(u - g - 0.5) < 0.4\}$ OR $\{u - g < 1.4$ AND $g - r < 0.25\}$; [100,759]
6. $-0.2 < 0.35(g - r) - (r - i) < 0.20$; [98,063]

For each star, the data analyzed in this work include the *ugriz* photometry, SDSS spectrum, and SSPP estimates of effective temperature (T_{eff}), metallicity ($[Fe/H]$), and gravity ($\log(g)$). The selected stars span the range of effective temperature from ~ 4500 K to ~ 9000 K (see below), and 99.4% have metallicity in the range $-3 < [Fe/H] < 0$ with a median of -1.0 . While the sample is dominated by main sequence stars (the median $\log(g)$ is 4.1 ± 0.44 dex), a small fraction of stars ($\sim 3\%$) have lower gravity estimates consistent with giants (see Figure 1).

2.3. The $g - r$ Color Binning

Stellar spectra are to the zero-th order similar to the Planck (black body) function controlled by the effective temperature; however, their variation of spectral line width and strength depend not only on effective temperature but also on metallicity and gravity. At a chosen effective temperature, the metallicity affects the strength of the spectral line and gravity can broaden or narrow the spectral line. In order to study these variations due to metallicity and gravity at a given effective temperature, we group the stars with SDSS spectra into 55 color bins with a width of 0.02 mag, in the range $-0.2 < g - r < 0.9$. As shown by Ivezić et al. (2008a), this color is strongly correlated with the effective temperature determined by the SSPP: 0.02 mag wide bin in the $g - r$ color roughly corresponds to one MK spectral subtype. The best-fit expression derived by Ivezić et al. (2008a),

$$\log(T_{eff}/K) = 3.882 - 0.316(g - r) + 0.0488(g - r)^2 + 0.0283(g - r)^3, \quad (1)$$

⁶See <http://www.sdss.org/dr6/products/spectra/spectroparameters.html>

achieves systematic errors below 0.004 dex and overall rms of 0.008 dex, within the $-0.3 < g - r < 1.3$ color range. The temperature range corresponding to the $g - r$ limits adopted here ($-0.2 < g - r < 0.9$) is 4,550 K – 8,850 K. The number of stars per $g - r$ bin ranges from 430 to 9104, with a median of 1571. The variation of the number of stars in a bin, the median apparent magnitude, metallicity, gravity, and the fractions of low-metallicity stars ($[Fe/H] < -1$) and giants ($\log(g) < 3$) are shown in Figure 2.

Most of the stars in our sample are main-sequence stars with $\log(g) > 3$ and $[Fe/H] > -1$. The impact of metallicity and gravity on stellar spectra, as well as the fraction of stars in the sample that are not main-sequence disk stars, varies with effective temperature, i.e., with the $g - r$ color. For the purposes of presentation, we single out two bins in $g - r$. For the 6156 stars in bin #23 ($0.24 < g - r < 0.26$) we expect a strong correlation between the $u - g$ color and metallicity, as discussed in detail by Ivezić et al. (2008a). We use this bin to compare the random errors for metallicity estimates obtained from the SSPP and obtained here using PCA. For bin #37, with $0.52 < g - r < 0.54$ and 8253 stars, the fraction of giants is near its maximum ($\sim 10\%$). This bin enables a study of correlations between $\log(g)$ and PCA eigencoeficients. The color range of bin #37 was deliberately targeted for SDSS spectroscopy because giant stars are good probes of distant halo structure. The distribution of stars from these two bins in the $\log(g)$ vs. $[Fe/H]$ metallicity diagram is compared to the full sample in Figure 3.

2.4. Principal Components Decomposition

For a thorough discussion of PCA and several of its various applications, we refer the reader to Connolly et al. (1995) and Yip et al. (2004). Briefly, PCA calculates eigenspectra, or characteristic averaged spectral shapes, from the input batch of spectra, and measures eigencoeficients that represent how strongly each eigenspectrum is present in a data spectrum. The PCA package we used was specifically developed for use with SDSS spectra (Yip et al. 2004). Before PCA decomposition occurs, the package shifts the spectra to their rest-frames (zero radial velocity) and rebins them to a common wavelength range. The spectra are then repaired in gappy regions (i.e. bad pixels or missing data) using the iterative KL-correction formalism developed by Connolly & Szalay (1999). The PCA code outputs eigenspectra, eigencoeficients, and repaired data spectra.

We investigated spectral decompositions using varying numbers of eigenspectra and found that the first four eigencomponents are sufficient to describe the observed spectra within the measurement noise (for a single spectrum). Figure 4 compares the median difference between the original and reconstructed spectra with the median noise in the original

spectra for bins #23 and #37. As shown, the spectra reconstructed using four eigencomponents are consistent with the original spectra to well within the typical measurement error. Furthermore, Figure 5 demonstrates that the difference between PCA decompositions based on four and six eigenspectra is minor (a few percent or less over most of the wavelength range).

This is a much smaller number of eigencomponents than typically required. For example, Bailer-Jones et al. (1998) used the first 10 components to expand stellar spectra in their sample. The reason for this difference is that here we individually treat very narrow bins of the $g-r$ color. In order to describe spectral variations due to metallicity and gravity in each bin (i.e., at nearly a constant effective temperature), a large number of eigencomponents is not necessary. Figures 6 and 7 show the eigenspectra for bins #23 and #37, respectively (the spectra are plotted in vacuum wavelengths).

3. Analysis of PC Decomposition Results

3.1. Correlations between eigencefficients and SSPP parameters

For each $g-r$ bin, the eigencefficients are expected to encode information about metallicity and gravity. Figures 8 and 9 demonstrate correlations between PCA eigencefficients (EC) and SSPP metallicity and gravity for bins #23 and #37. For bin #23, a correlation between metallicity and EC2, EC3, and EC4, is present in the data, while there is no correlation with gravity. Note, however, that this bin includes only a small fraction of giant stars (3% with $\log(g) < 3$). For bin #37, eigencefficients are correlated with both metallicity and gravity. However, as demonstrated in Figure 3, the metallicity and gravity are correlated for stars in this bin (due to SDSS spectroscopic target selection criteria, for more details see Yanny et al. 2009), and thus it is not clear which parameter is driving the correlation with eigencefficients. A sample of high-metallicity giants or low-metallicity dwarfs is required to decouple the effects of these two parameters. Such stars are not present in the sample; the former are mostly nearby disk stars and thus too bright and saturated in SDSS data, while the latter are distant halo stars and too faint to be included in the SDSS spectroscopic survey (Ivezić et al. 2008a).

For a more quantitative investigation of the correlation observed in bin #23, we fit straight lines to the three relationships between metallicity and eigencefficients 2, 3, and 4 (best-fit parabolas lead to the same conclusions). We then average the three best-fit metallicity estimates obtained using each eigencefficient and compare the result to values reported by the SSPP (Figure 10). The resulting bimodal distributions look similar, though

one could argue that the values determined with PCA have slightly larger random errors (by about 20%) than the official SDSS values because the distinction between the two peaks in metallicity distribution is somewhat erased.

For another comparison of the two metallicity estimators, we use the $u-g$ color obtained from imaging data. As shown by Ivezić et al. (2008a), for stars with blue $g-r$ colors, spectroscopic metallicity is strongly correlated with the $u-g$ color (see the top panel in Figure 11). They estimate that the random photometric metallicity errors are even smaller than the random metallicity errors determined by the SSPP from SDSS spectra (a random $u-g$ error of 0.02 mag induces a metallicity error in $[Fe/H]$ that varies from 0.02 dex at $[Fe/H] = -0.5$ to 0.11 dex at $[Fe/H] = -1.5$). Hence, for stars from bin #23, we can compare the spectroscopic metallicities determined by PCA and by the SSPP using the scatter around an average fit (see the bottom panel in Figure 11; a best-fit parabola leads to the same conclusion); the better metallicity determination would have less scatter. We find essentially identical error behavior, which suggests that the parameter precision obtained by PCA is comparable to that achieved by the SSPP for stars with $0.2 < g-r < 0.3$.

3.2. Mean Stellar Spectra Determined by PCA

One of the PCA products derived in this work is a set of high signal-to-noise gap-repaired mean spectra at each $g-r$ color. We show a stack of 55 such spectra in Figures 12 and 13. The variation of absorption line strengths and overall continuum shape with the $g-r$ color are easily discernible. For example, the depth of the $H\alpha$ line steadily decreases as the $g-r$ color becomes redder.

In addition to mean spectra that roughly correspond to stars with *median* metallicity and gravity in a given $g-r$ bin, the remaining eigenspectra can be used to generate high signal-to-noise spectra for *any* combination of basic stellar parameters (effective temperature, metallicity, and gravity), within the parameter space probed by SDSS. Hence, given an arbitrary spectrum, one can attempt a low-dimensional fit using our library of eigenspectra, which we make publicly available⁷.

⁷<http://www.astro.washington.edu/users/ivezic/rmcgurk/PCAPublic.shtml>

3.3. Variation of Mean Stellar Spectra with Metallicity and Gravity

The mean spectra shown in Figures 12 and 13 are averaged over metallicity and gravity distributions in the corresponding color bins. The small variations of stellar spectra with metallicity and gravity, at a fixed $g - r$ color, can be studied by drawing eigencoefficients from their observed distribution in a given bin. Given the quality of SDSS spectra and the high signal-to-noise ratio of the mean spectra (due to large number of stars per bin), these variations can be studied in great detail. An example of such a study is shown in Figures 14 and 15, where we contrast low- and high-metallicity stars from bin #23, and low (giants) and high (dwarfs) $\log(g)$ stars from bin #37. For example, the sensitivity of the Ca triplet (around $\sim 8600 \text{ \AA}$) to both metallicity and gravity is easily discernible (this wavelength range is exploited by the RAVE and Gaia surveys).

4. Summary

We have applied Principal Component Analysis (PCA) to $\sim 100,000$ stellar spectra obtained by the SDSS. After binning the sample using the $g - r$ color to study line variation at a nearly constant effective temperature as a function of the metallicity and gravity, we find that the first four eigenspectra fully capture the observed spectral variations in each bin (within the noise in individual SDSS spectra). We analyze correlations between our PCA eigencoefficients and SEGUE Stellar Parameters Pipeline (SSPP) metallicity, and then use these correlations to measure metallicity. We find similar performance between the PCA-measured metallicity and the SSPP metallicity. This similarity suggests that *random errors of SSPP parameters are just about as small as the signal-to-noise ratios of SDSS spectra allow.*

We make publicly available the resulting high signal-to-noise mean spectra and the other three eigenspectra for all 55 color bins. These data can be used to generate high quality spectra for an arbitrary combination of effective temperature, metallicity, and gravity, within the parameter space probed by SDSS. The utility of such spectra is wide and varied. Most obvious applications include searching for unusual spectra, training of various spectral classification methods, and color synthesis in arbitrary optical photometric systems, as well as various educational programs.

Acknowledgments

We are thankful to Andy Connolly and Ching-Wa Yip for making their PCA code

available to us, and to Robert Lupton for suggesting this project. We acknowledge support by NSF grants AST-615991 and AST-0707901.

Funding for the SDSS and SDSS-II has been provided by the Alfred P. Sloan Foundation, the Participating Institutions, the National Science Foundation, the U.S. Department of Energy, the National Aeronautics and Space Administration, the Japanese Monbukagakusho, the Max Planck Society, and the Higher Education Funding Council for England. The SDSS Web Site is <http://www.sdss.org/>.

The SDSS is managed by the Astrophysical Research Consortium for the Participating Institutions. The Participating Institutions are the American Museum of Natural History, Astrophysical Institute Potsdam, University of Basel, University of Cambridge, Case Western Reserve University, University of Chicago, Drexel University, Fermilab, the Institute for Advanced Study, the Japan Participation Group, Johns Hopkins University, the Joint Institute for Nuclear Astrophysics, the Kavli Institute for Particle Astrophysics and Cosmology, the Korean Scientist Group, the Chinese Academy of Sciences (LAMOST), Los Alamos National Laboratory, the Max-Planck-Institute for Astronomy (MPIA), the Max-Planck-Institute for Astrophysics (MPA), New Mexico State University, Ohio State University, University of Pittsburgh, University of Portsmouth, Princeton University, the United States Naval Observatory, and the University of Washington.

REFERENCES

- Abazajian, K., & Sloan Digital Sky Survey, f. t. 2008, ArXiv e-prints
- Allende Prieto, C., Beers, T. C., Wilhelm, R., Newberg, H. J., Rockosi, C. M., Yanny, B., & Lee, Y. S. 2006, *ApJ*, 636, 804
- Allende Prieto, C., et al. 2007, ArXiv e-prints, 710
- Bailer-Jones, C. A. L., Irwin, M., & von Hippel, T. 1998, *MNRAS*, 298, 361
- Beers, T. C., et al. 2006, *Memorie della Societa Astronomica Italiana*, 77, 1171
- Connolly, A. J., & Szalay, A. S. 1998, in *IAU Symposium, Vol. 179, New Horizons from Multi-Wavelength Sky Surveys*, ed. B. J. McLean, D. A. Golombek, J. J. E. Hayes, & H. E. Payne, 376–+
- Connolly, A. J., & Szalay, A. S. 1999, *AJ*, 117, 2052

- Connolly, A. J., Szalay, A. S., Bershad, M. A., Kinney, A. L., & Calzetti, D. 1995, *AJ*, 110, 1071
- Covey, K. R., et al. 2007, *AJ*, 134, 2398
- Eisenstein, D. J., et al. 2001, *AJ*, 122, 2267
- . 2006, *ApJS*, 167, 40
- Fan, X. 1999, *AJ*, 117, 2528
- Finlator, K., et al. 2000, *AJ*, 120, 2615
- Gunn, J. E., et al. 2006, *AJ*, 131, 2332
- Ivezić, Ž., et al. 2008a, *ArXiv e-prints*, 804
- Ivezić, Ž., Tyson, J. A., Allsman, R., Andrew, J., Angel, R., & for the LSST Collaboration. 2008b, *ArXiv e-prints*, 805
- Ivezić, Ž., Vivas, A. K., Lupton, R. H., & Zinn, R. 2005, *AJ*, 129, 1096
- Lee, Y. S., et al. 2007a, *ArXiv e-prints*, 710
- . 2007b, *ArXiv e-prints*, 710
- Lenz, D. D., Newberg, J., Rosner, R., Richards, G. T., & Stoughton, C. 1998, *ApJS*, 119, 121
- Richards, G. T., et al. 2002, *AJ*, 123, 2945
- Schlegel, D. J., Finkbeiner, D. P., & Davis, M. 1998, *ApJ*, 500, 525
- Sirko, E., et al. 2004, *AJ*, 127, 899
- Smolčić, V., et al. 2004, *ApJ*, 615, L141
- Strauss, M. A., et al. 2002, *AJ*, 124, 1810
- Yanny, B., et al. 2009, *AJ*, 137, 4377
- Yip, C. W., et al. 2004, *AJ*, 128, 2603
- York, D. G., et al. 2000, *AJ*, 120, 1579

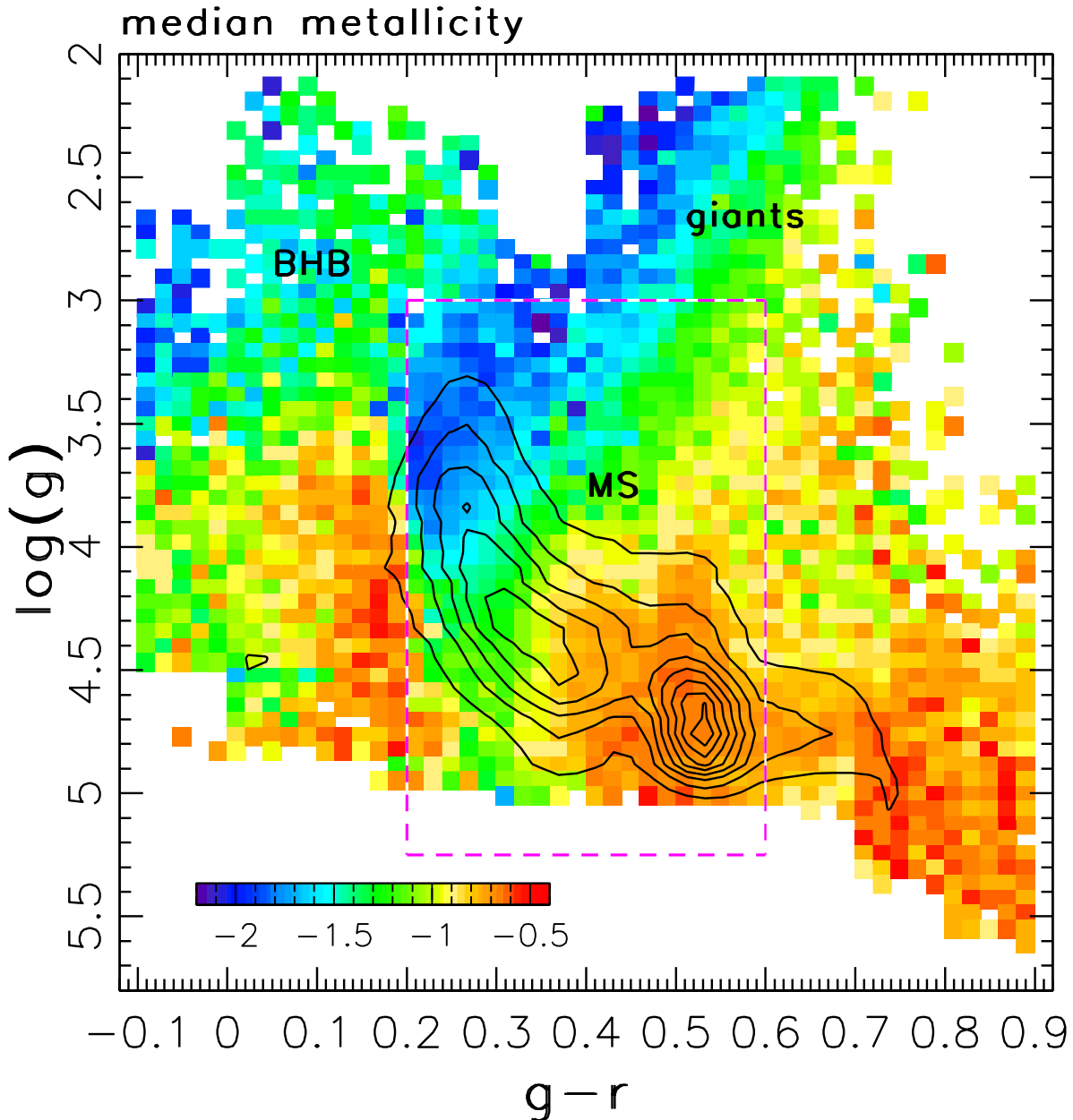


Fig. 1.— The linearly-spaced contours show the distribution of $\sim 100,000$ stars with $g < 19.5$ from the SDSS DR6 spectroscopic sample in the $\log(g)$ vs. $g - r$ plane. The multi-modal distribution is a result of the SDSS target selection algorithm. The color scheme shows the median metallicity in all 0.02 mag by 0.06 dex large pixels that contain at least 10 stars (according to the legend shown in the bottom left corner). The fraction of stars with $\log(g) < 3$ (giants) is 4%, and they are mostly found in two color regions: $-0.1 < g - r < 0.2$ (BHB stars) and $0.4 < g - r < 0.65$ (red giants). They are dominated by low-metallicity stars ($[Fe/H] < -1$). The dashed lines roughly outline the main-sequence (MS) region, see Ivezić et al. (2008a).

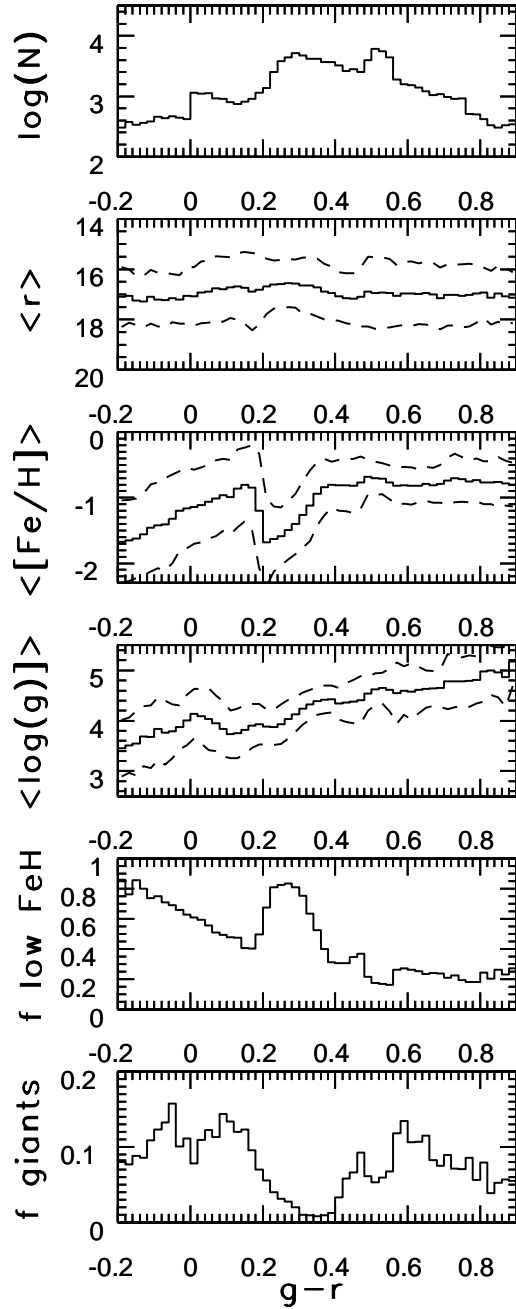


Fig. 2.— Top to bottom: The solid lines show the variation of the number of stars in a given $g-r$ bin, the median apparent r band magnitude, metallicity, gravity, and the fraction of low-metallicity stars ($[Fe/H] < -1$) and giants ($\log(g) < 3$). Dashed lines show the 1σ envelope around the medians. Stars with $g-r > 0.2$ are dominated by main sequence stars, and the bluer stars are dominated by blue horizontal branch stars, RR Lyrae stars, and blue stragglers. The approximate $g-r$ colors for several MK spectral types (luminosity class V) are taken from Covey et al. (2007).

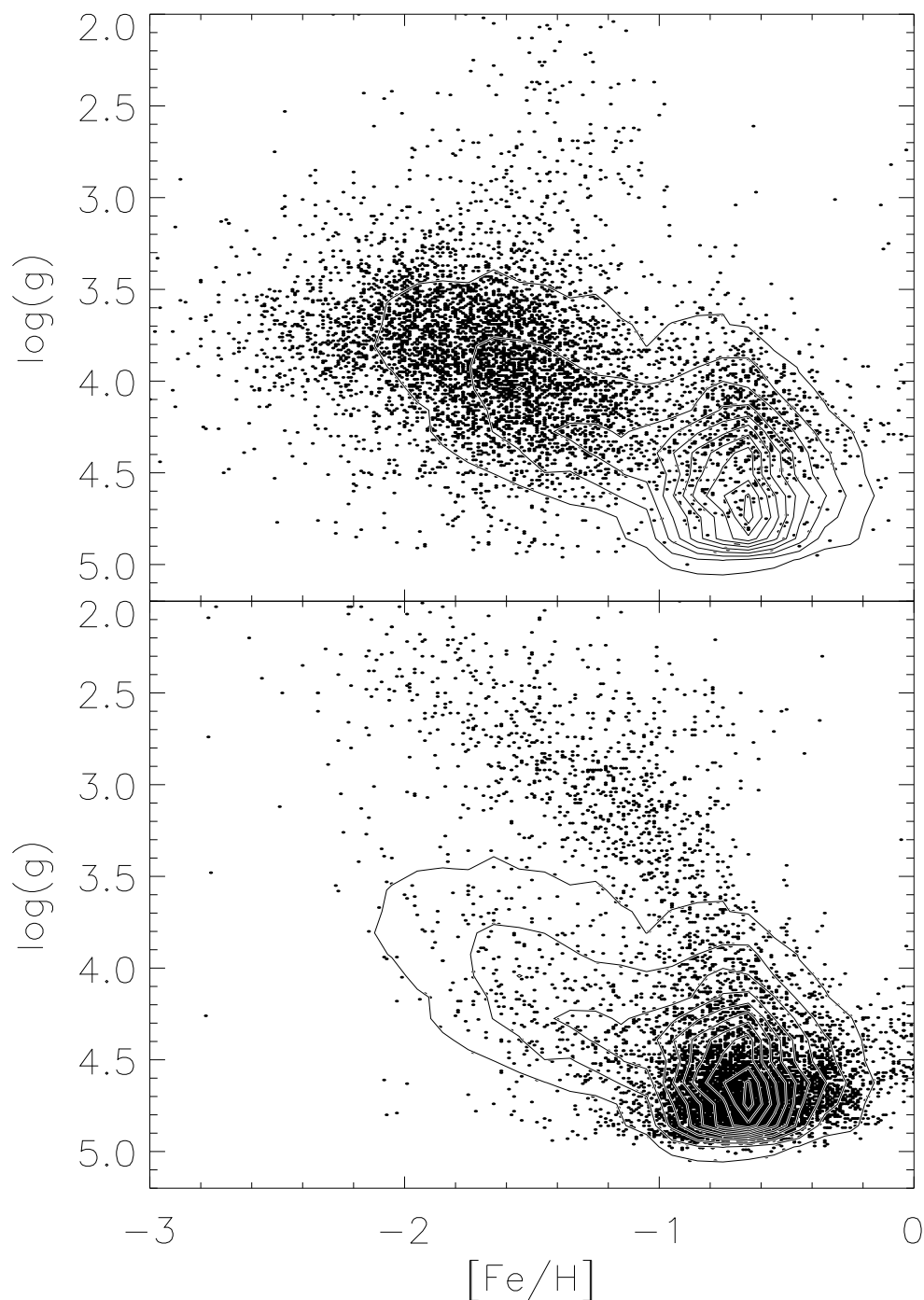


Fig. 3.— The bivariate metallicity-gravity distribution for two color bins. In both panels, the linearly-spaced contours show the $\log(g)$ vs. $[Fe/H]$ distribution of the $\sim 100,000$ stars in the analyzed sample. The symbols in the top panel show stars from bin #23, and the bottom panel shows stars from bin #37. Bin #37 ($\log(g) < 3.5$ and $[Fe/H] < -1$) contains many low-metallicity giant stars.

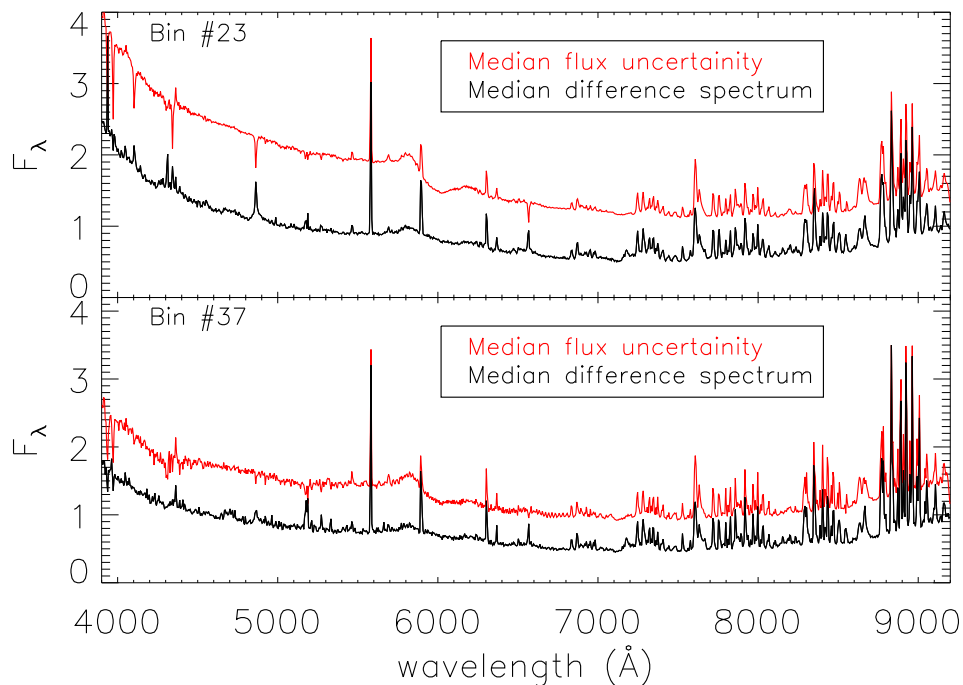


Fig. 4.— The median difference spectra and median noise spectra for bins #23 (top) and #37 (bottom). The median difference spectra are black and the median noise spectra are red. The median difference spectra were constructed by taking the absolute value of the difference of each original spectrum and its reconstructed spectrum, and then taking the median of the difference spectra in vacuum wavelength bins of width 5\AA . We took the median of the noise spectra in similar wavelength bins to create the median noise spectra. We demonstrate in both bins that the use of four eigencoefficients reconstructs the original spectra to within the measurement noise.

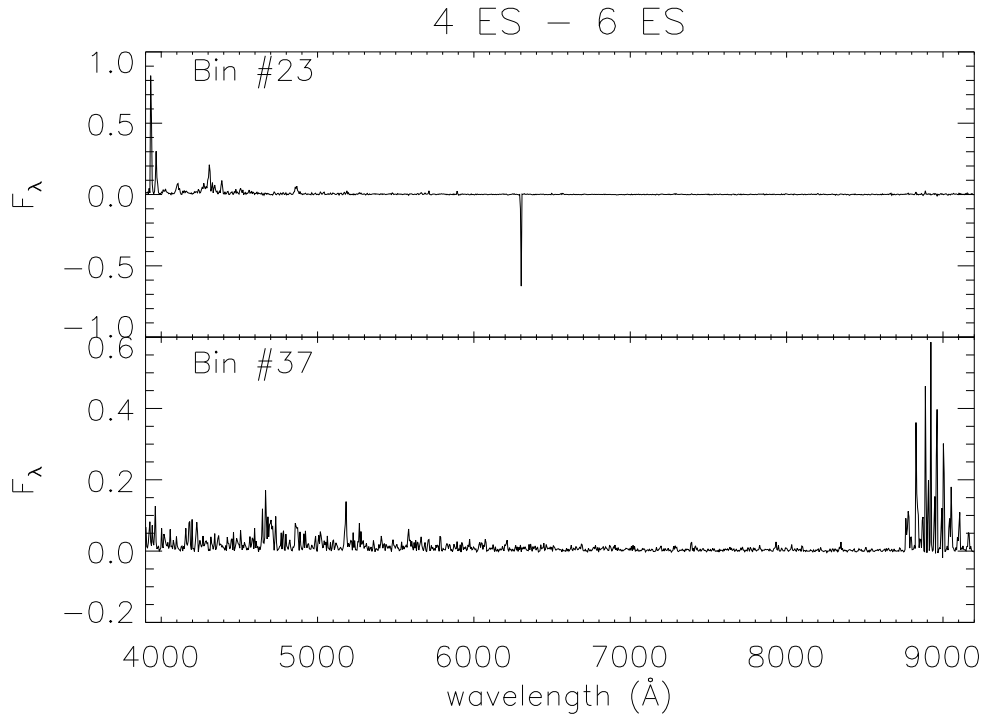


Fig. 5.— A comparison of the median difference spectra for PCA decompositions based on four and six eigenspectra for bins #23 (top) and #37 (bottom). The median difference spectra were constructed by taking the absolute value of the difference of each original spectrum and its reconstructed spectrum, and then taking the median. The results for PCA decomposition based on four eigenspectra are shown in Figure 4. These two panels show the difference between the results from Figure 4 and analogous median difference spectra for six eigencomponents.

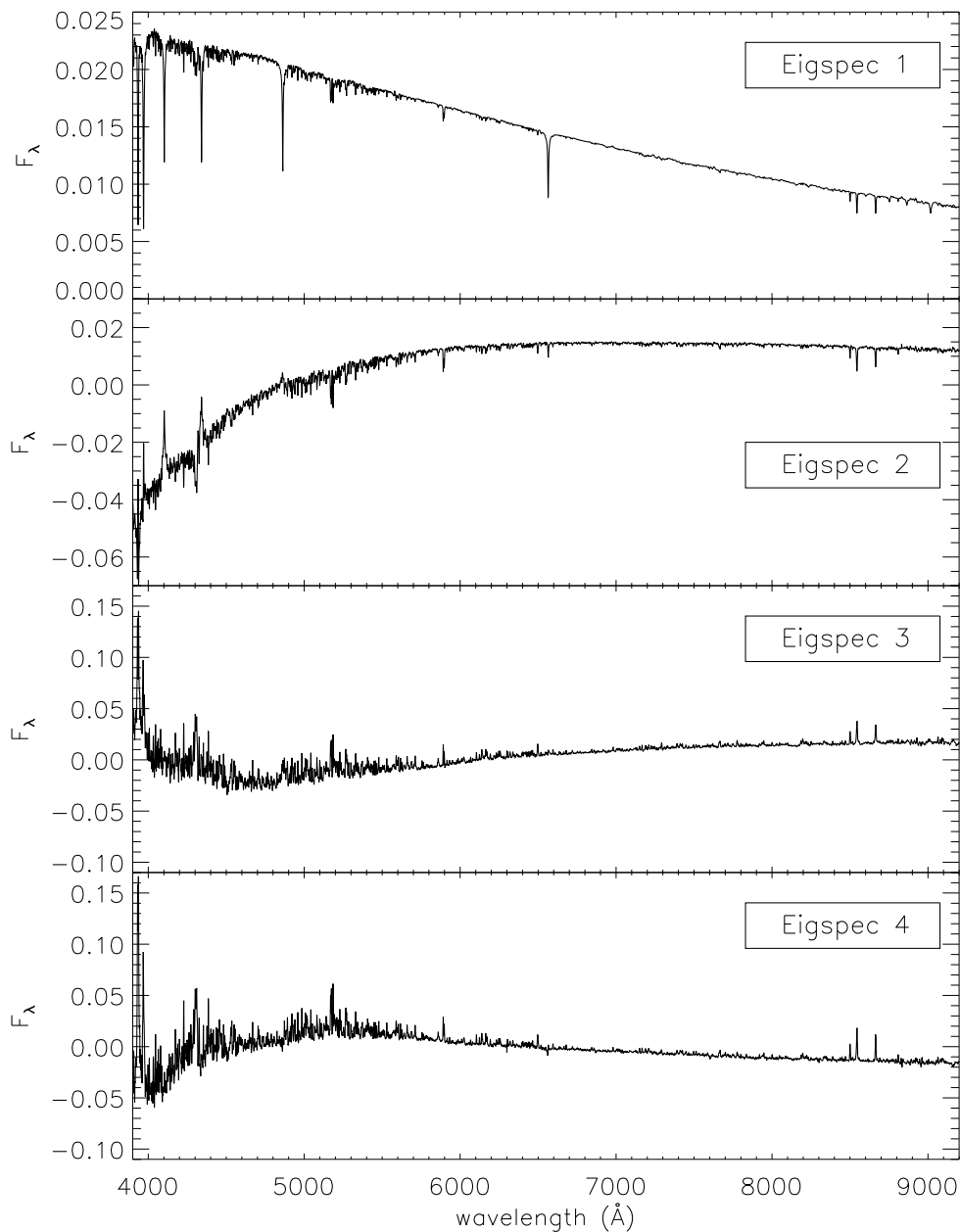


Fig. 6.— The four eigenspectra (F_λ) generated for the 6156 stars in bin #23 ($0.24 < g - r < 0.26$), plotted at vacuum wavelengths. The first eigenspectrum closely resembles a metal-poor ($[Fe/H] \sim -1.5$) subdwarf. The variation of spectra in this bin is expected to be dominated by the variation of stellar metallicity.

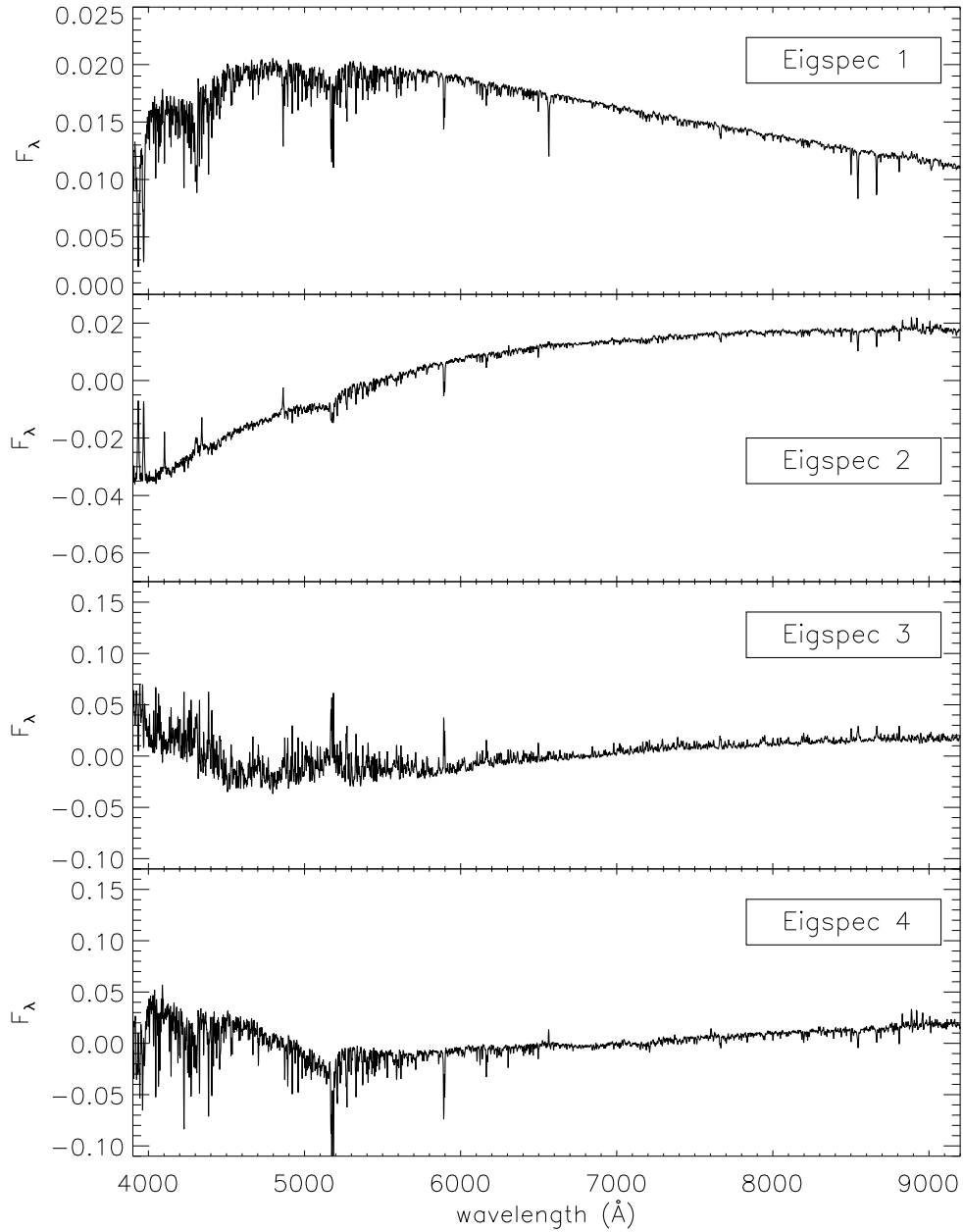


Fig. 7.— The four eigenspectra generated for the 8253 stars in bin #37 ($0.52 < g - r < 0.54$), plotted at vacuum wavelenths. The first eigenspectrum closely resembles a metal-rich ($[Fe/H] \sim -0.7$) dwarf. The variation of spectra in this bin is expected due to a high fraction of giant stars (which presumably also have lower metallicity than the majority of stars in the sample).

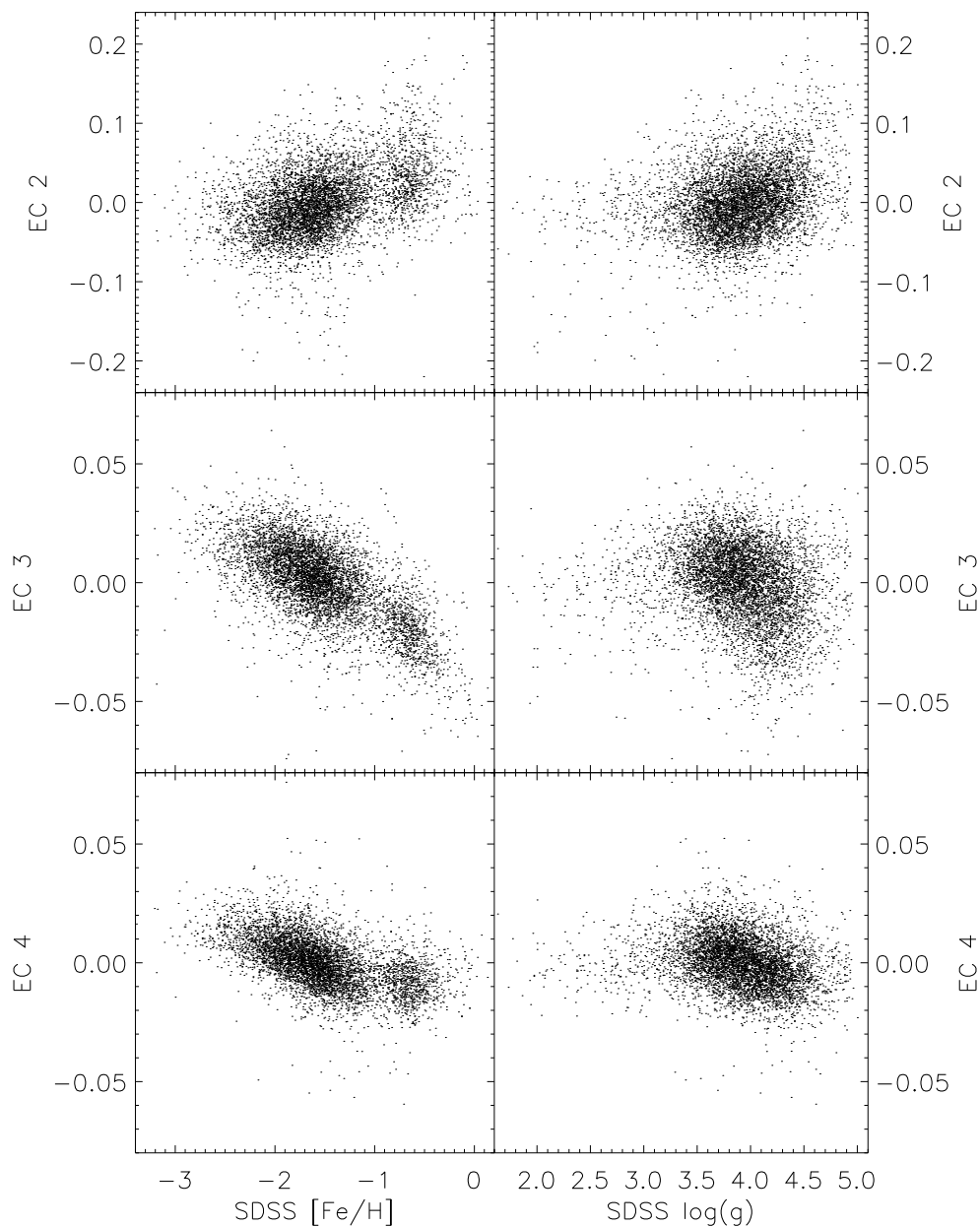


Fig. 8.— Eigencoefficients for bin #23, corresponding to eigenspectra shown in Figure 6, shown as a function of metallicity (left column) and gravity (right column) computed by SSPP. Note a small fraction of giant stars ($\log(g) < 3$) and a correlation between metallicity and EC2, EC3, and EC4. The bimodal metallicity distribution reflects the SDSS targeting algorithm and significantly different metallicity distributions for halo ($[Fe/H] < -1$) and disk ($[Fe/H] > -1$) stars.

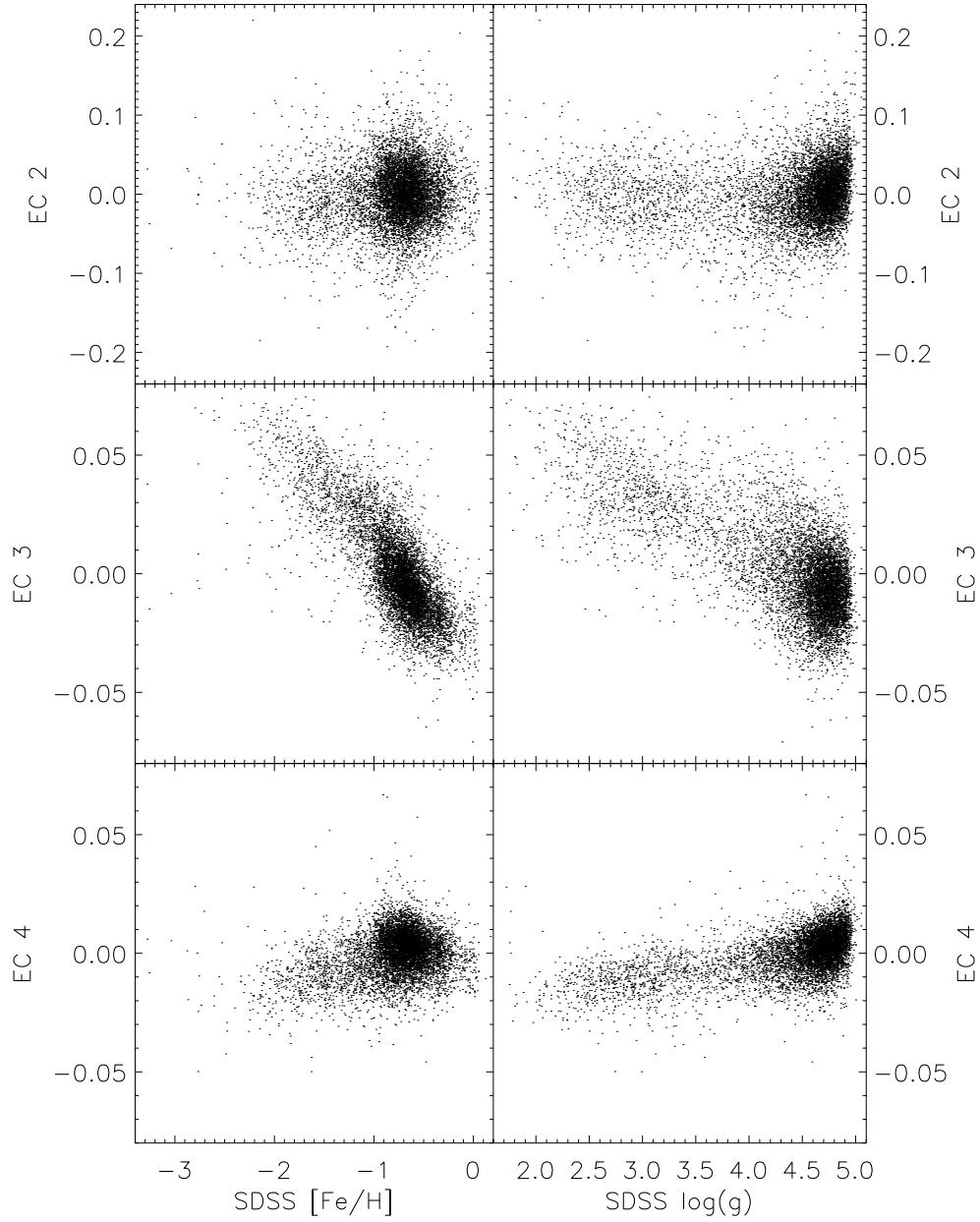


Fig. 9.— Eigencoefficients for bin #37, corresponding to eigenspectra shown in Figure 7, shown as a function of metallicity (left column) and gravity (right column) computed by SSPP. Note a much larger fraction of giant stars than in Figure 8. The eigencoefficients seem correlated with both metallicity and gravity. The sample does not include high-metallicity giants.

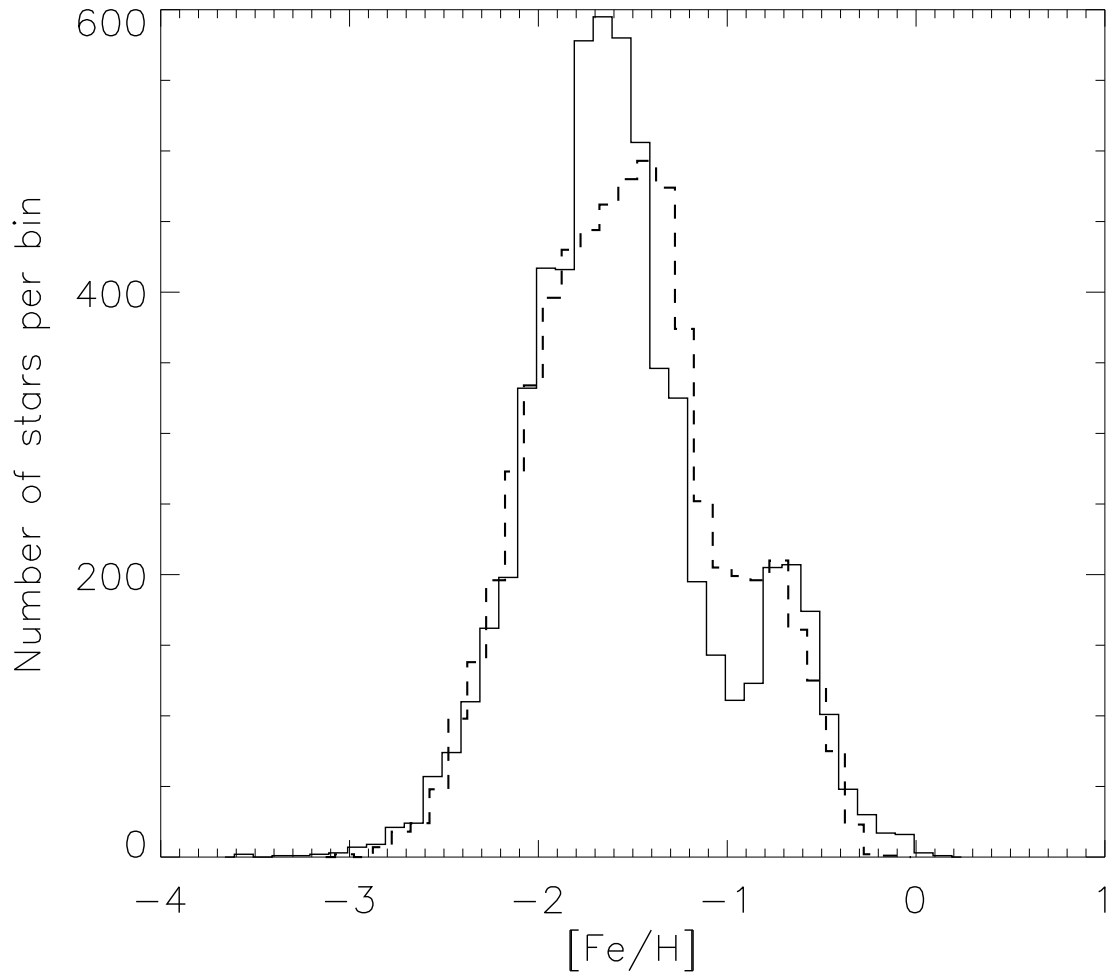


Fig. 10.— A comparison of the metallicity estimates obtained by the SDSS SSPP pipeline (solid histogram) and our PCA-based estimates (dashed histogram).

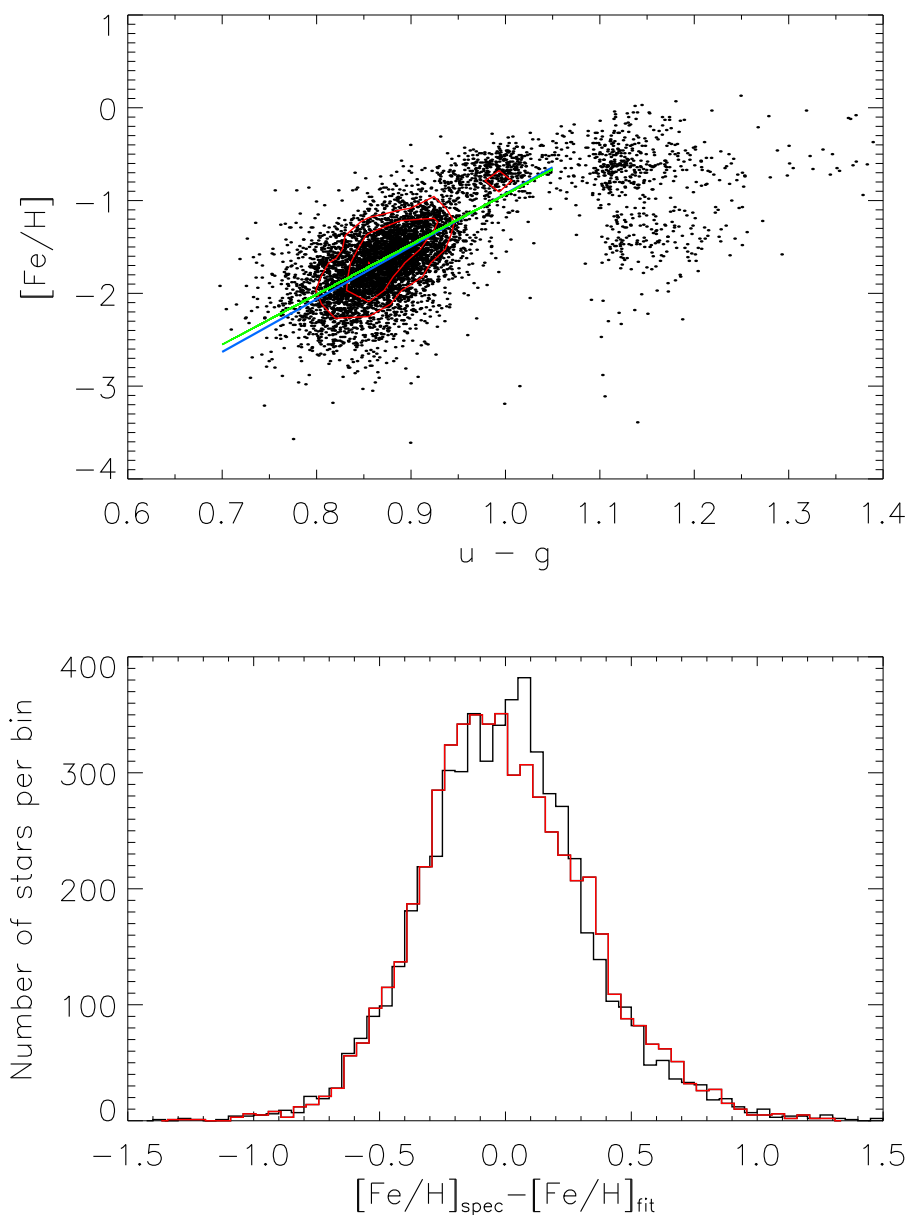


Fig. 11.— An independent test of two metallicity estimators based on a correlation of metallicity and the $u - g$ color. In the top plot, black points illustrate SSPP-measured metallicities, while the red contours illustrate our new metallicity measurements. The green and blue lines are the best-fit lines to the two datasets, respectively the SSPP fit and the new PCA fit. The bottom plot illustrates the scatter of each data set around the best-fit lines, with black being the SSPP data and red being the new metallicity data.

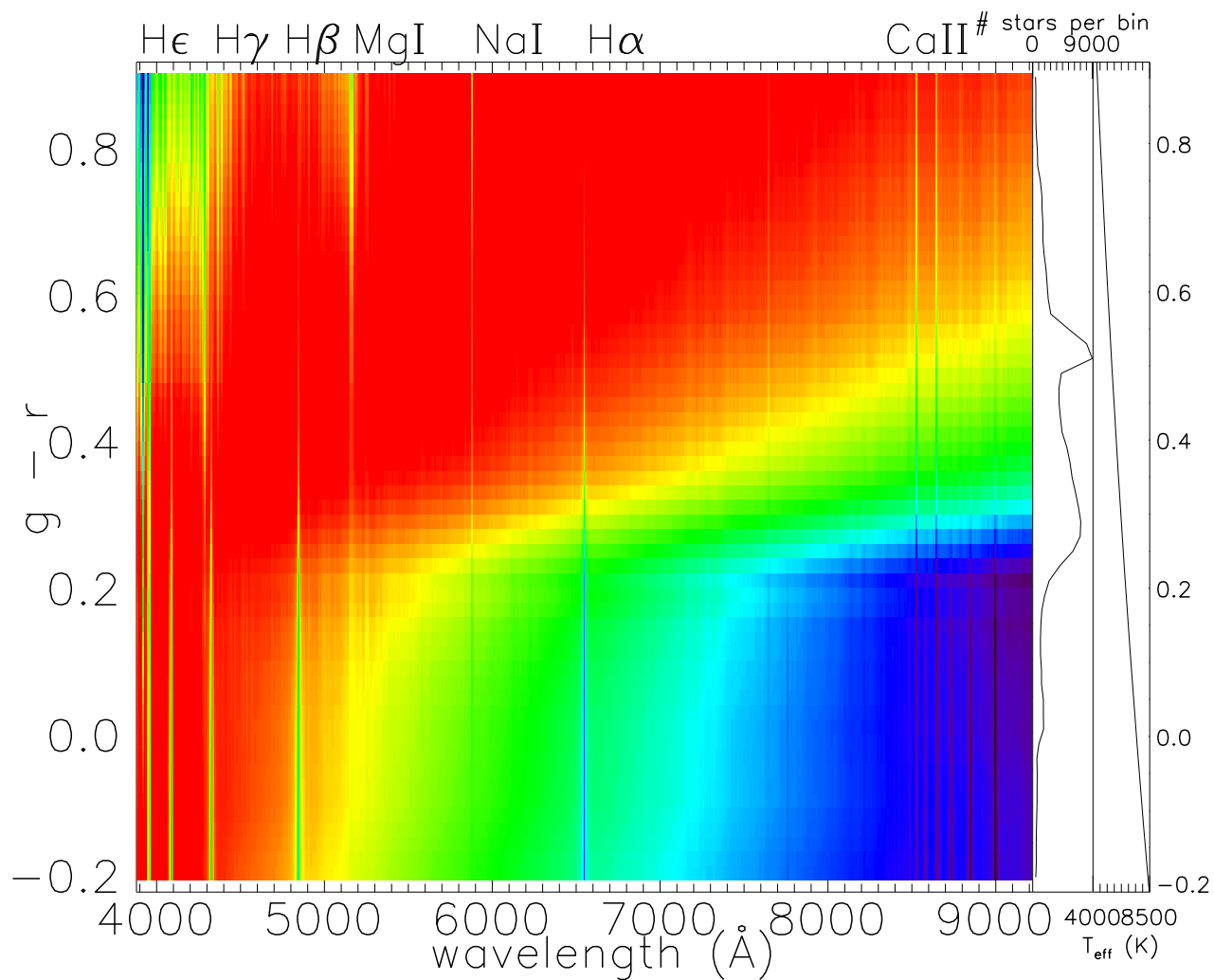


Fig. 12.— The progression of mean spectra (F_λ) plotted in vacuum wavelengths as a function of the $g-r$ color determined using PCA. The values increase logarithmically from blue to red. The two panels on the right side show the mean number of stars per 0.02 mag wide $g-r$ bin, and the corresponding median effective temperature. A few spectral absorption lines are marked on top.

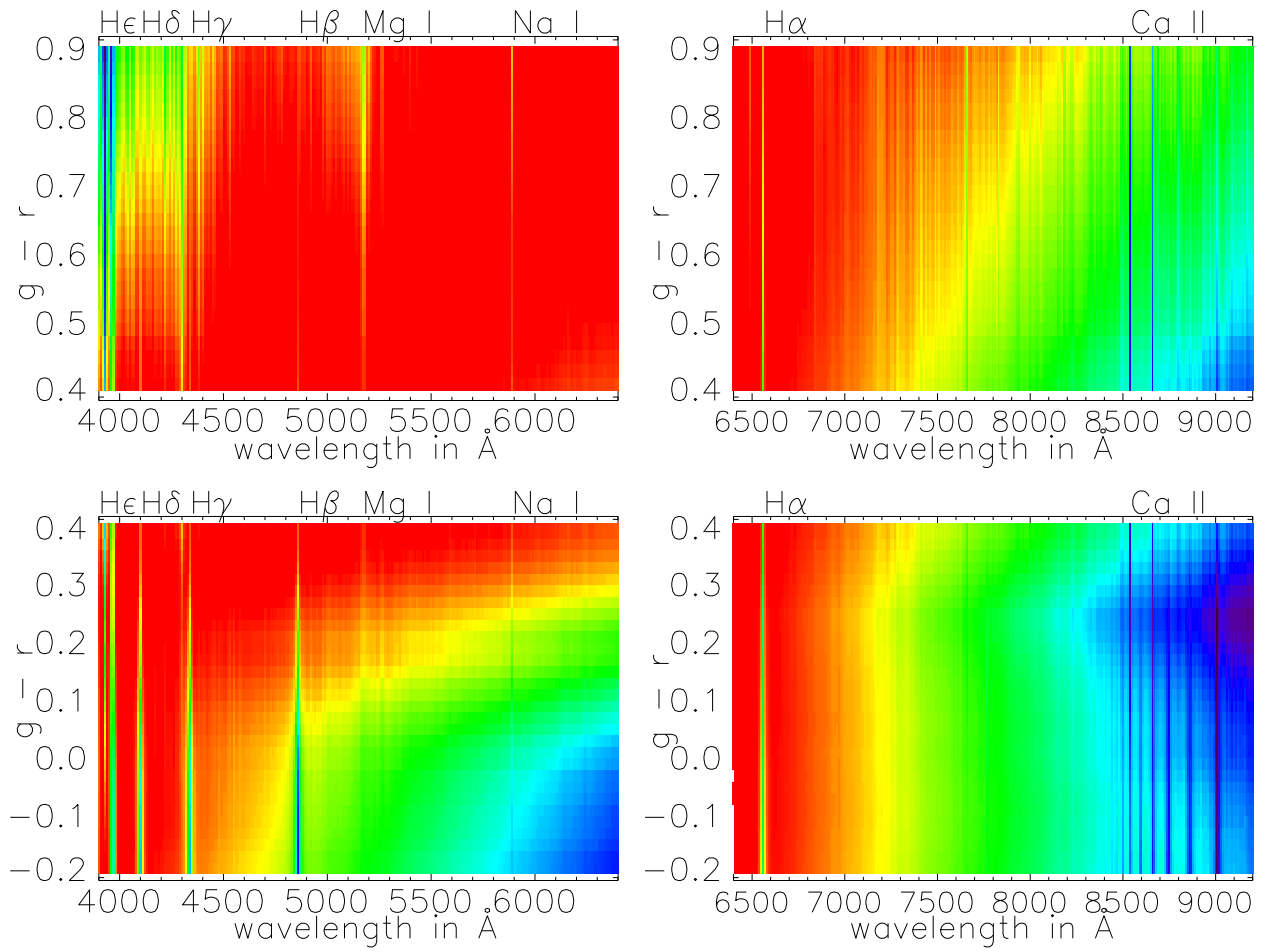


Fig. 13.— Analogous to Figure 12, except that the wavelength range and the $g - r$ range are split in halves and each panel is separately color-coded to increase the contrast of spectral features.

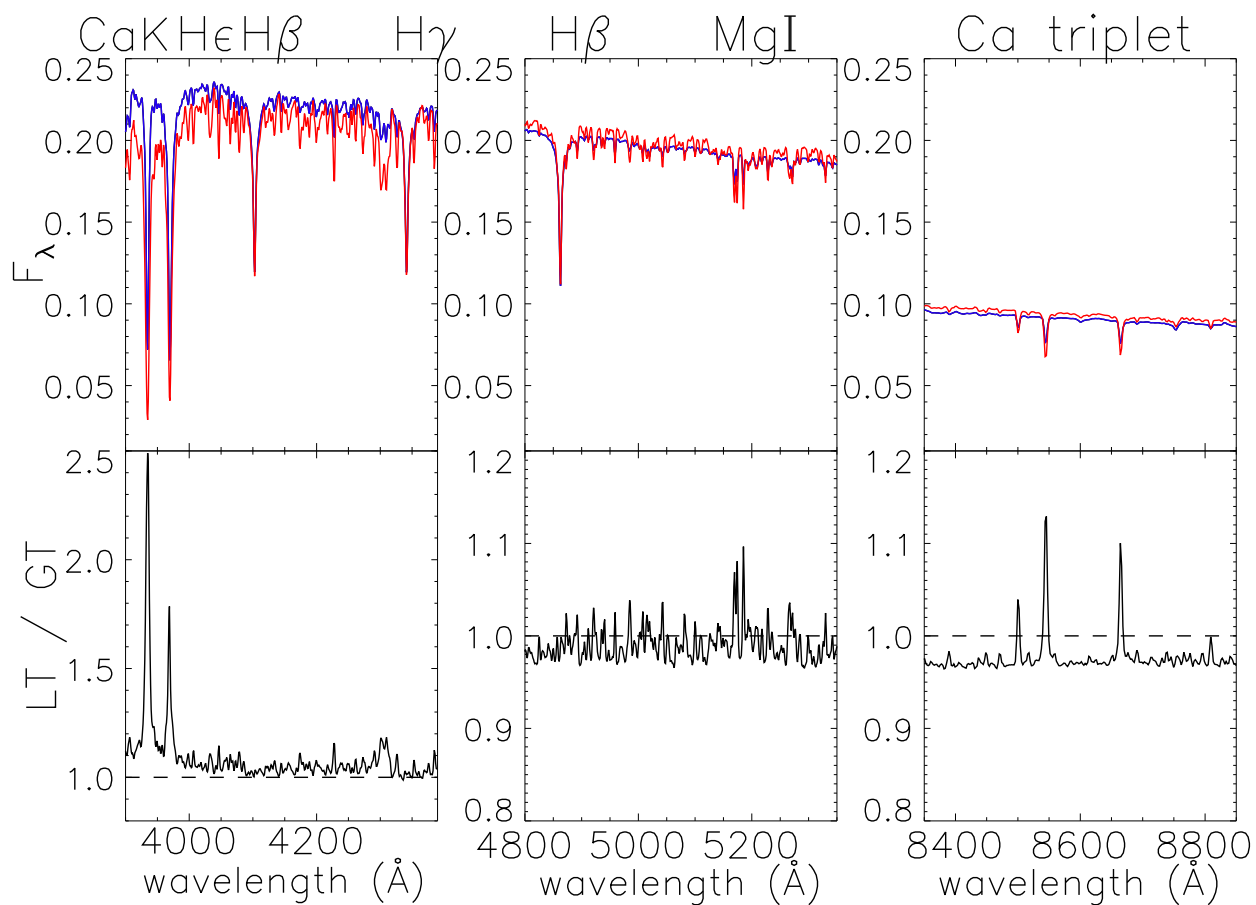


Fig. 14.— The top panels show two reconstructed spectra in three characteristic vacuum wavelength ranges for bin #23. The spectra are generated using mean eigencoefficients of the two clumps separated by $[Fe/H] = -1.05$ (see Fig. 8; the blue line corresponds to the clump with $[Fe/H] < -1.05$ and the red line to the more metal-rich clump). The bottom panels show the ratio of the low-metallicity ($[Fe/H] \sim -1.5$) and the high-metallicity spectrum ($[Fe/H] \sim -0.6$).

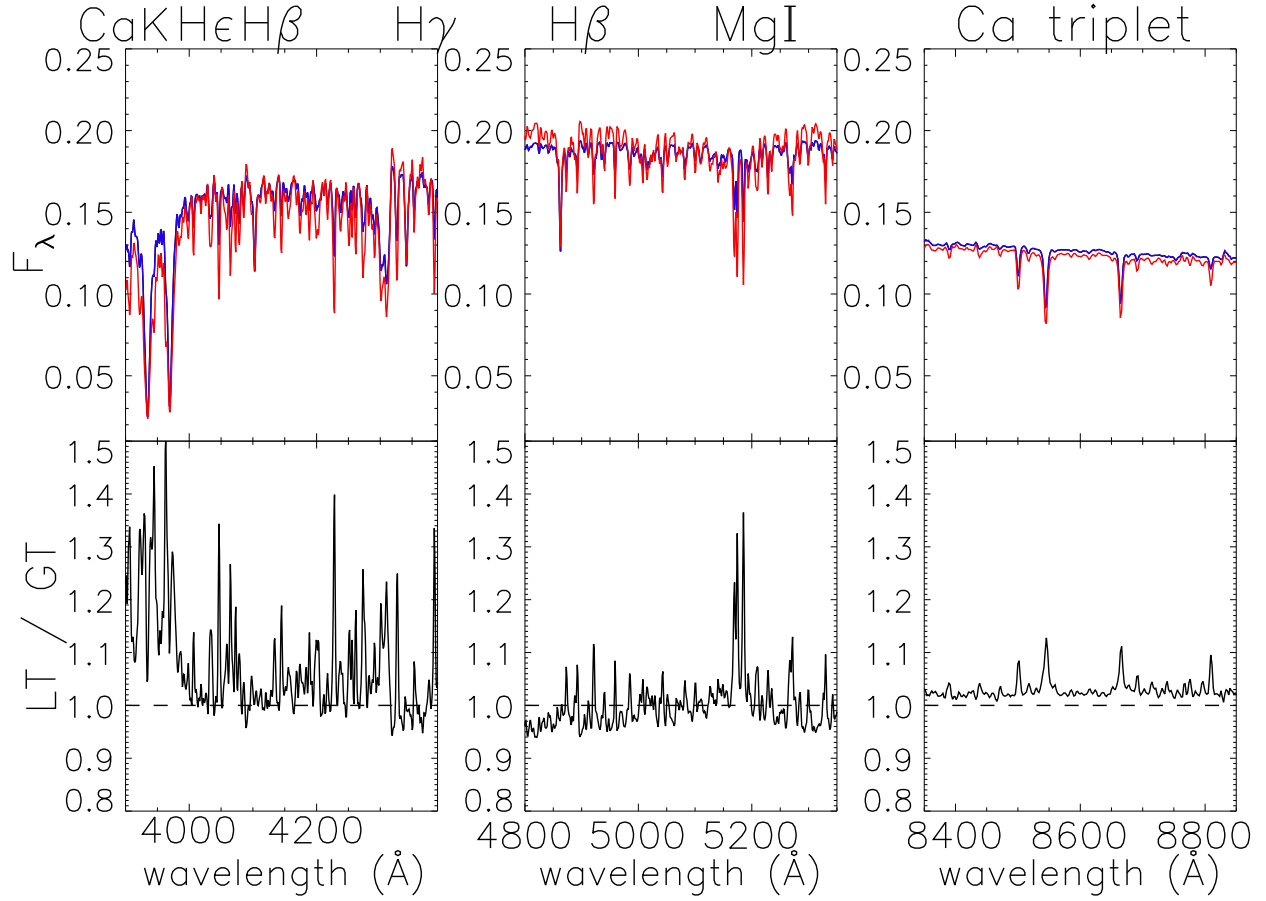


Fig. 15.— Similar to Figure 14, except that spectra are reconstructed for bin #37. The two reconstructed spectra are generated using mean eigencoefficients for the clump with $\log(g) < 3.7$ (blue line), and the clump with $\log(g) > 3.7$ (red line), see Fig. 9 for the distribution of eigencoefficients.